

Converging-diverging shock-driven instabilities along soft hydrogel surfaces

Daniel Pickard,^{1,2} Dmitro Martynowych,^{3,2} Jet Lem ^{3,2} Anwar Koshakji ^{1,2} Shaoting Lin,⁴ Xuanhe Zhao,⁴ Keith Nelson,^{3,2} Bianca Giovanardi ^{1,2,5} and Raul Radovitzky^{1,2}

¹*Department of Aeronautics and Astronautics, Massachusetts Institute of Technology, Cambridge, Massachusetts 02139, USA*

²*Institute for Soldier Nanotechnologies, Massachusetts Institute of Technology, Cambridge, Massachusetts 02139, USA*

³*Department of Chemistry, Massachusetts Institute of Technology, Cambridge, Massachusetts 02139, USA*

⁴*Department of Mechanical Engineering, Massachusetts Institute of Technology, Cambridge, Massachusetts 02139, USA*

⁵*Faculty of Aerospace Engineering, Delft University of Technology, 2628 CD Delft, Netherlands*



(Received 2 June 2021; accepted 6 January 2023; published 7 February 2023)

Intense surface eruptions are observed along the curved surface of a confined cylindrical film of hydrogel subject to laser-induced converging-diverging shock loading. Detailed numerical simulations are used to identify the dominant mechanisms causing mechanical instability. The mechanisms that produce surface instability are found to be fundamentally different from both acoustic parametric instability and shock-driven Richtmyer-Meshkov instability. The time scale of observed and simulated eruption formation is much larger than that of a single shock reflection, in stark contrast to previously studied shock-driven instabilities. Moreover, surface undulations are only found along external, as opposed to internal, soft solid boundaries. Specifically, classic bubble surface instability mechanisms do not occur in our experiments and here we comment only on the new surface undulations found along the outer boundary of solid hydrogel cylinders. Our findings indicate a new class of impulsively excited surface instability that is driven by cycles of internal shock reflections.

DOI: [10.1103/PhysRevE.107.L022601](https://doi.org/10.1103/PhysRevE.107.L022601)

Introduction. Soft solids such as human connective tissue are subjected to large amplitude stress waves in a variety of medical procedures such as shock wave lithotripsy, which is common for the removal of kidney stones [1–4], and histotripsy cancer treatments [5–7]. Soft matter response to high strain rates and loading conditions is also relevant to the study of blast induced injuries of human and animal tissues [8–10]. Beyond practical applications, soft material dynamics have been found to exhibit a number of instabilities of theoretical interest, including Rayleigh-Taylor [11–13], Faraday [14], parametric [15–17] and Richtmyer-Meshkov instabilities [18–20]. Many of these mechanisms are closely related to fluid dynamic instabilities. However, soft solids can produce a number of distinctive instability patterns which fluids do not [21,22].

In this Letter, we describe such a dynamic instability that was discovered while studying the response of hydrogels to converging shock loading. In contrast to previous work on shock driven Richtmyer-Meshkov instabilities [18,23,24], in our experiments surface undulations develop on a time scale much larger than that of the initial shock dynamics and form after multiple internal reflections. Our impulse driven experiment precludes the possibility of classic forced parametric resonance within the specimen, and we show via numerical simulation that surface instability is instead controlled by nonlinearity in the material response to shock loading.

Our experimental setup, depicted schematically in Fig. 1, is a 50- μm -thick specimen of a soft hydrogel sandwiched between two 300- μm -thick glass plates. The gel is a polyacrylamide network prepared by mixing 10 ml aqueous solutions

of 12% wt. acrylamide (A8887 Sigma-Aldrich), 5% wt. Epson 522 printer ink, 2.5% wt. sodium alginate (A2033 Sigma-Aldrich), 0.023% wt. N,N-methylenebisacrylamide (146072 Sigma-Aldrich) and 0.043% wt. ammonium persulphate (A3678 Sigma-Aldrich). 0.03% wt. N,N,N',N'-tetramethylethylenediamine (T9281 Sigma-Aldrich) is added prior to pouring the mixture onto a glass slide. The mixture is covered with a second slide and crosslinked for an hour using 254 nm UV light exposure with an energy deposition rate of 6 W/m^2 . The N,N-methylenebisacrylamide acts as a crosslinker. Ammonium persulphate is a thermal initiator. N,N,N',N'-tetramethylethylenediamine accelerates the crosslinking. Printer ink is needed to absorb the laser energy that generates shock waves. A laser pulse of 8-ns duration containing 230 μJ of energy is focused on a 180 μm -diameter ring of the specimen using our experimental setup previously described in Refs. [25,26]. The laser energy melts material along the circumference of the cylinder, thereby separating it from the remainder of the hydrogel sheet, and excites an intense pressure wave that propagates toward its center. A high-frame-rate camera (SIMX 16, Specialized Imaging) is used to acquire 16 images spaced by 0.6 μs . As an illuminating probe, we use a 640-nm-wavelength laser (SI-LUX640, Specialized Imaging) of 30 μs pulse duration, which is longer than the total time required to acquire the 16 frames with the high-frame-rate camera. Figure 2 shows the images obtained.

Consistent with prior studies of converging shocks in water, cavitation is observed early on in the center of the disk and is a consequence of dilatational stresses exceeding the tensile strength of the gel after the shock initially focuses

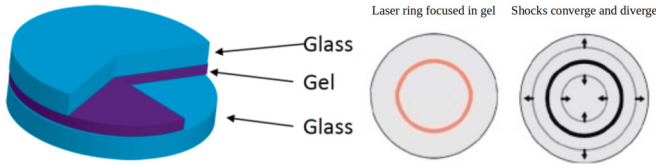


FIG. 1. Schematic of hydrogel specimen sandwiched between glass plates (left), detail of the initial circular 180 μm -diameter laser ring (center) and waves emanated from laser-ablated ring (right).

and begins to diverge [27]. At much larger times, localized deformation patterns in the form of surface eruptions nucleate, grow and decay between 3 and 8 μs . No undulations develop along the external boundary of the ablation zone, though a variety of instabilities are known to occur along such curved external gel domains due to steady gas pressure [28] or inertial effects [21]. The specimen inside the laser ring does not show evidence of inelastic deformation or damage in its final state. Surface instability along only the internal boundary of a toroidal laser ablation ring has not yet been reported in soft matter, and we note that these effects were not observed in analogous experiments using water [27].

In order to provide insight into the underlying physics, we conducted detailed finite element simulations of our experiment using our research code Σ MIT [29]. For simplicity, we only model the domain inside the circular ablation region using a circular mesh with initial radius R_0 equal to 90 μm consisting of 34 480 first order, plane strain triangular elements. The volumetric constitutive response of the gel is modeled using the Tait equation of state which is justified given the material’s large water content ($\sim 85\%$). The two required model parameters define the infinitesimal bulk modulus at the origin and the degree of stiffening in the nonlinear response. In our simulation, we adopt a bulk modulus at the

origin κ of 2 GPa and a stiffening exponent $\bar{\gamma}$ of 6.15 [30], which correspond approximately to the volumetric response of water. A neo-Hookean elastic model is adopted to describe the deviatoric stress response, which has been shown to effectively describe the quasistatic response in hydrogels [13,31–35]. The required model parameter is selected so that the shear modulus at the origin μ matches the stiffness of our specimen in its reference configuration at 5 KPa. The elastic strain energy function W is given in terms of the Jacobian J of the deformation gradient \mathbf{F} and the first invariant I of the right Cauchy-Green tensor \mathbf{C} :

$$W = \frac{\kappa}{\bar{\gamma} - 1} \left(\frac{J^{-\bar{\gamma}}}{\bar{\gamma}} + J - \frac{\bar{\gamma} + 1}{\bar{\gamma}} \right) + \frac{\mu}{2} \left(\frac{I}{J^{2/3}} - 3 \right). \quad (1)$$

The elastic first Piola-Kirchhoff stress is computed as

$$\mathbf{P} = \left(-\frac{\kappa}{\bar{\gamma} - 1} (J^{-\bar{\gamma}} - J) - \frac{\mu}{3} \frac{I}{J^{2/3}} \right) \mathbf{F}^{-T} + \frac{\mu}{J^{2/3}} \mathbf{F}. \quad (2)$$

It bears emphasis that the material model considered here accounts for nonlinear volumetric material response. Both Rayleigh-Taylor and parametric instabilities of soft solids have been studied extensively assuming either isochoric deformations [16,21] or the low Mach number approximation of Keller and Miksis [36–38]. Our modeling framework captures these instabilities in the incompressible and acoustic regimes respectively, but our interest in shock driven experiments motivates this more general approach.

It was found that the simulations are able to capture the mechanisms of instability on the surface without the need for explicitly describing the complex laser energy deposition process, and instead by simply applying a mechanical load along the boundary. Specifically, the boundary conditions applied consisted of a square pressure pulse duration t_{pulse} of 8 ns on the cylinder surface with an amplitude P_{pulse} of 2.0 GPa, which corresponds to an energy deposition of approximately 75 μJ . We estimate that approximately a third of the laser energy in the experiment is injected into the hydrogel cylinder, and have found that loading conditions of this intensity accurately reproduce experimental observations. As commonly required in simulations of shock-wave propagation, we add artificial viscosity for shock stabilization using linear and quadratic viscosity parameters of $c_1 = 1.0$ and $c_L = 0.1$ [39]. We utilize second-order explicit Newmark time integration with mass lumping to evolve the dynamic fields in time [40,41]. The time step is selected to maintain a CFL number of one half which guarantees numerical accuracy and stability.

Simulation Results. In order to visualize the sequence of interesting events that take place during the various reflections of the ensuing stress waves, we monitor the evolution of the minimum and maximum radial displacements on the free surface, Fig. 3. For comparison purposes we plot a scalar metric of instability amplitude $\bar{A} = \frac{r_{\text{max}} - r_{\text{min}}}{R_0}$ on the right axis. r_{max} and r_{min} denote the maximum and minimum radial displacement along the domain boundary. We also provide representative snapshots of the evolution of the relevant mechanical fields at times of particular interest in Figs. 4–6. Animated videos containing the full -dynamic evolution of these fields are provided in the Supplemental Material [42].

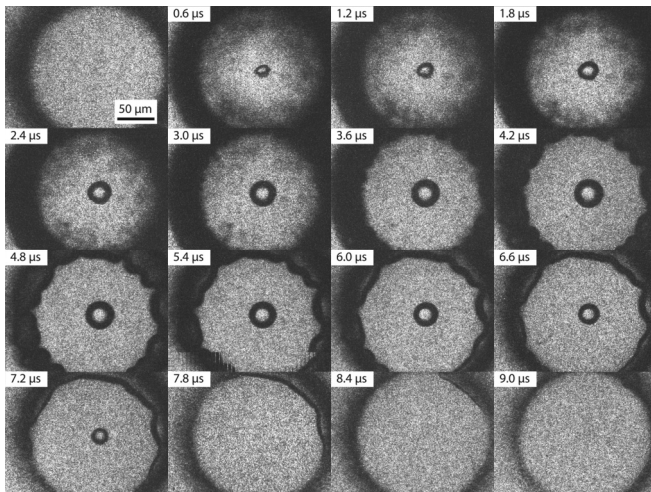


FIG. 2. Time sequence of images obtained in laser-shock experiment on hydrogel. The images are taken every 0.6 μs . The dark region around the edge of the pictures corresponds to the laser-ablated hydrogel material. The images clearly show the formation of a cavitation bubble at around 0.6 μs which disappears at around 7.2 μs . Pronounced unstable deformation patterns appear on the surface at some time between 2.4 and 3.0 μs .

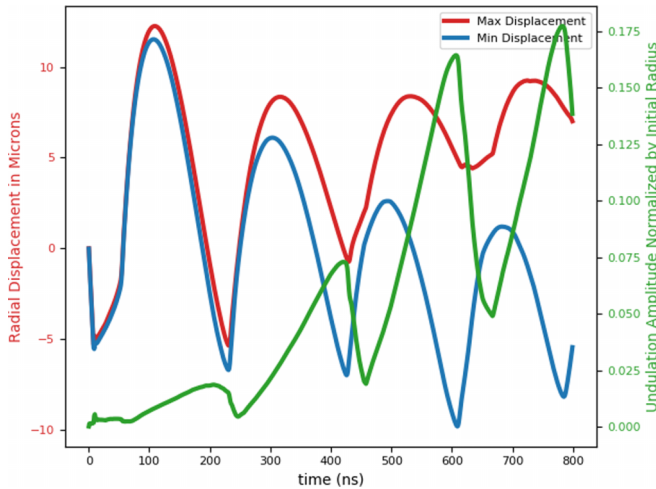


FIG. 3. Maximum (red) and minimum (blue) radial displacement along the boundary plotted over time. The difference between the two has been normalized by the initial radius of 90 μm and is shown in green.

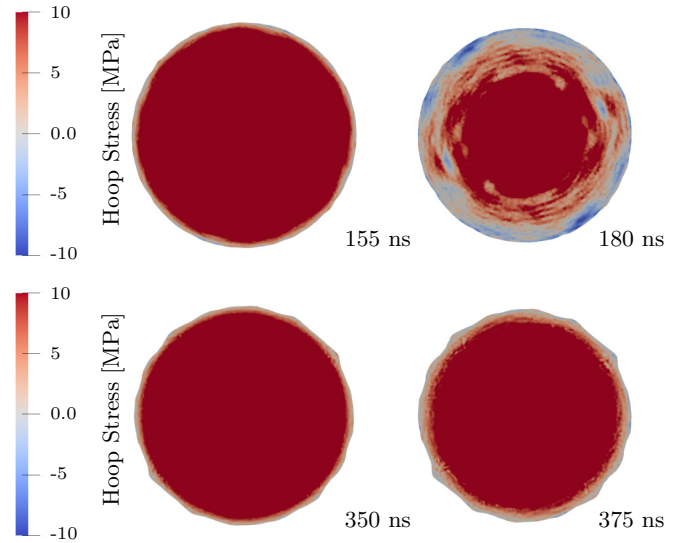


FIG. 6. Top: Hoop stress on a ± 10.0 MPa scale at 155 and 180 ns. Bottom: Hoop stress on a ± 10.0 MPa scale at 350 and 375 ns.

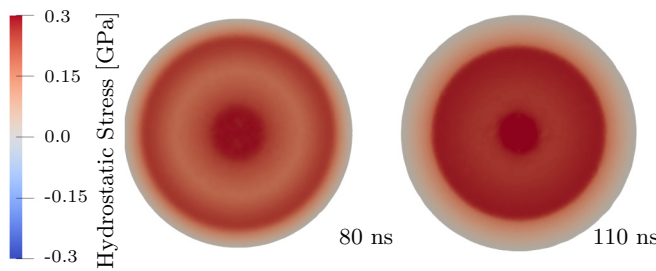


FIG. 4. Hydrostatic stress contours plotted at times 80, 110 ns on a ± 0.3 GPa scale. Observe the tensile wave traveling inward.

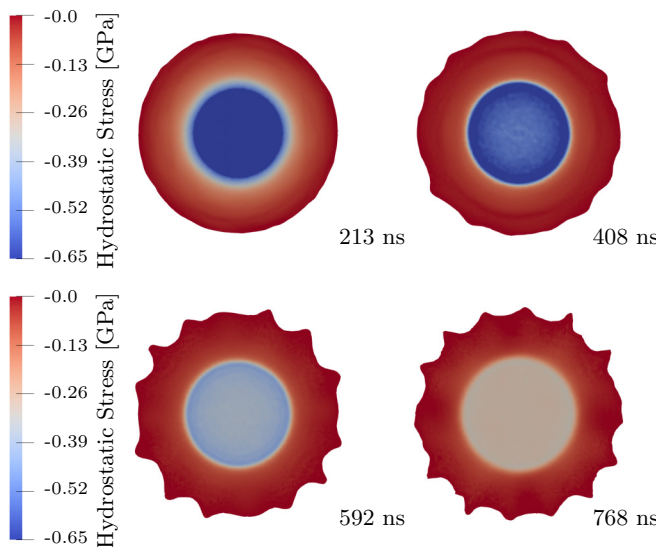


FIG. 5. Hydrostatic stress contours on a scale from -0.65 GPa to zero at 213, 408, 592, and 768 ns. The diverging shock is visible in these frames taken 20 ns prior to each of the final four reflections. The simulations capture eruption formation.

The initial hydrostatic stress wave shocks up as it converges toward the center. Convergence occurs at 29 ns at which point the entire domain is in compression. As the stress wave diverges, the center is placed under tension, a condition that persists until 202 ns.

At 55 ns, the shock wave reflects off the boundary, accelerating it outward in the radial direction, and the free surface in turn reflects a tensile stress wave toward the center of the domain. Figure 4 illustrates the circular tension wave at 80 ns. The tensile wave moves far slower than the shock because the bulk modulus decreases when under tension. It takes 147 ns for the tension wave to focus into the center of the domain while the shock traversed the same distance in 26 ns. The central tensile region and the reflected stress wave join into a common, shrinking tensile core. Outside this region the hydrostatic stress is still positive, but significantly smaller.

At 202 ns, the tensile region contracts to a point and the continued inward motion of material causes hydrostatic compression at the center which drives a second diverging shock. This concludes one complete cycle of the pressure wave. Subsequent pressure wave cycles consist of a tensile phase followed by a radially expanding shock. Converging shocks do not occur in later cycles and are only present at the start of the simulation. Additional shock reflections are found at 233, 428, 612, and 788 ns.

Discussion. Figure 3 demonstrates that the boundary radial displacement initially remains nearly homogeneous, but axial symmetry breaks down over time as evidenced by the diverging maximum and minimum radial displacement curves. The consequent increase in \bar{A} indicates the formation of localized deformation features or surface eruptions around the circumference which are shown in Fig. 5. Both figures show that the surface undulation amplitude grows with each cycle of wave reflection and reaches up to 15% of the initial radius on the fourth cycle before starting to decrease due to viscous dissipation. This is remarkably similar to the surface eruptions observed experimentally. We note that the

characteristic wavelength nondimensionalized by the sample radius ranges between 0.37 and 0.45 in both our simulations and our experimental observations, which corresponds to between 14 and 17 clearly visible undulations along the boundary.

Figure 3 shows that the breakdown of symmetry (when the maximum and minimum displacements diverge) starts at around 80 ns after the first inflexion point of the radial surface displacement, i.e., when the boundary acceleration changes signs although the surface is still moving outward. The incipient inward acceleration toward the heavier material is responsible for the onset of the instability, but in contrast to the inertial effects driving Rayleigh-Taylor type mechanisms in converging shock settings [43–47] it is the tensile release wave, not the compressive shock that nucleates surface undulations. The effect also appears similar to the classic Richtmyer-Meshkov instability, which occurs when a fluid interface is rapidly accelerated by the passage of a shock wave from the less dense toward the more dense fluid [23,24], but in stark contrast with the Richtmyer-Meshkov instability our simulations show interface acceleration caused by radial tension not by shock compression. In fact, in our experiments and simulations the shocks actually propagate from the middle toward the lighter laser ablated region, which provides a surface regularizing effect responsible for the rapid decreases of the undulation amplitude \bar{A} with each reflection, Fig. 3. The detailed animations provided in the Supplemental Material [42] confirm both the tensile wave-driven radially inward surface acceleration as the mechanism for nucleation of localized deformation, as well as the stabilizing effects of outward-moving shock reflections.

An analysis of the evolution of the circumferential (hoop) stress exposes a second mechanism that contributes to the growth of the surface instability, namely the development of a compressive circumferential stress, which occurs when the boundary is pulled radially inward, Fig. 6. As in other types of elastic instabilities where the main mechanism driving the onset and growth is compression in directions tangent to a free surface [48], we find that hoop compression plays a key role in generating large scale eruptions. In particular, the destabilizing compressive hoop stresses develop under radial tension which indicates significant deviatoric stress and results in surface rotations and undulations. For instance, in Fig. 6 at 180 ns, the radial displacement is negative along the free surface and hence the circumferential strain is negative, but the radial stress remains tensile. In Fig. 3 it is apparent that the radial displacement plots continue to curve downward due to radial tension even after the displacement and hoop strain first attain negative values. Boundary radial stresses do not become compressive and push the domain outward until just prior to the shock arrival. The maximum hoop compression that occurs due to radial tension along the boundary is 11 MPa at 180 ns and we continue to observe MPa-scale hoop compression in subsequent pressure cycles. Although these hoop stresses are small compared to the GPa-scale pressures arising from shock compression, they are still large when compared to the 5 KPa shear modulus of the soft hydrogel.

The simulations capture growth of many wave numbers during the initial oscillation cycles when undulation formation is driven primarily by radially inward acceleration, see Fig. 7.

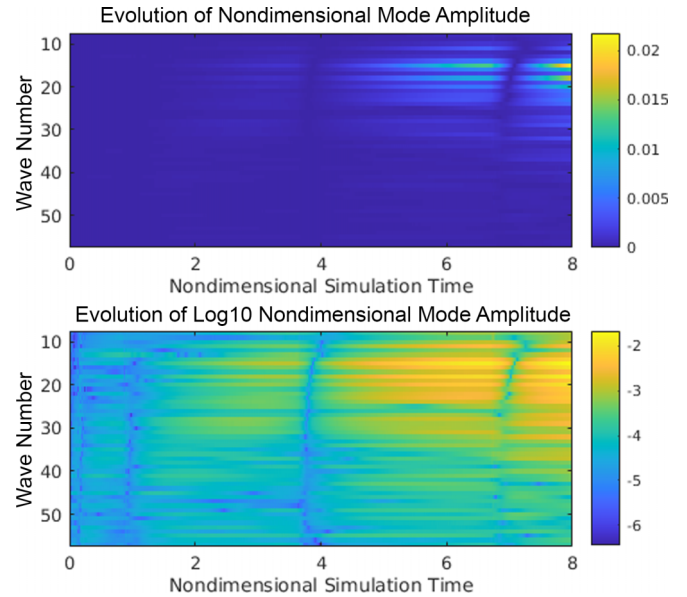


FIG. 7. Evolution of the Fourier modes of the surface undulation (normalized by the domain radius) plotted against nondimensional time $\bar{t} = t/R_0\sqrt{\kappa/\rho}$.

In this figure, the color represents the amplitude of the Fourier modes of the nondimensional boundary radial displacement field plotted along the vertical axis as a function of the nondimensional time \bar{t} plotted along the horizontal axis. As a convenient measure of the time scale we normalize by the time for acoustic propagation from the boundary to the center of the domain: $\bar{t} = \frac{t}{\tau}$ where $\tau = R_0\sqrt{\frac{\rho}{\kappa}}$. Though many modes are excited by inertial effects, the large scale undulations we showcase in this Letter are clearly of a moderate wave number on the order of 20. We find that the hoop compression effect preferentially amplifies these intermediate wave numbers at later times once inertial effects have dissipated. A detailed order parameter study which includes Refs. [49–56] is provided in the Supplemental Material and underscores this finding [42].

According to our analysis, cylindrical Rayleigh-Taylor or parametric instabilities as reported in Refs. [15,57–59] may develop regardless of the scale of the hydrostatic stress because these instabilities do not require nonlinear volumetric material response, but the instability reported in this paper requires sufficiently large pressures and wave dispersion upon shock reflection. Richtmyer-Meshkov instabilities do require a nonlinear equation of state but develop due to baroclinic effects induced by compressive shock waves. Even in the context of reshocked Richtmyer-Meshkov instability, where first a converging and then a diverging wave drive instability growth, the domain does not typically enter the tensile phase of the pressure cycle [18,60]. In our case, we have considered many cycles of internally reflecting large amplitude stress waves and have found that the overall period of oscillations and emergence of large elastic surface instabilities is controlled by the tensile material response when in the strongly nonlinear range.

The key features of the simulations are also evident in our experimental observations. A soft material’s critical cavitation stress scales with shear stiffness [61,62], which precludes water from sustaining the large amplitude tensile stress cycles

that are needed to form this new class of surface instabilities. The novel mechanism is not found in water in our recent experiments or in previous studies [27]. Additionally, experimental undulations form only along one side of the laser ring because the external surface of the ablation zone does not experience oscillatory loading due to internal wave reflections and does not develop compressive hoop stress. Rather, the external hydrogel is placed under circumferential tension by the thermal expansion of material inside the laser ablation ring. Hoop compression along the external surface of a curved laser ablation zone does not typically develop on a submicrosecond time scale for gel cavities with characteristic lengths of $\sim 100\ \mu\text{m}$ [37] and consequently such curved surfaces form instabilities slower than those reported here [21]. Additionally, the time scale of both observed and simulated instability growth considered here is more than an order of magnitude faster than the oscillation period typically used to generate forced parametric instability of comparably sized bubbles in soft gels [15]. High frequency forced vibrations are challenging to excite uniformly due to wave scattering,

but our laser-driven experiment generates high frequency and highly nonlinear oscillations inside the hydrogel cylinder. Our accompanying elastodynamic model demonstrates that cycles of large amplitude waves can rapidly induce surface instabilities in materials possessing both sufficient softness and tensile strength.

Conclusion. In summary, we have observed and simulated a different nonlinear elastodynamic instability which is driven by radial acceleration and circumferential hoop compression. Materials exhibiting this instability must possess sufficient ultimate strength to sustain large amplitude nonlinear pressure waves. It should be emphasized that this instability has only been described recently since it occurs along the boundary of shocked soft solids with small radii of curvature. The experimental setup considered here is ideally suited for exploring this regime of mechanical response.

Acknowledgments. The authors gratefully acknowledge support from the U.S. Army through the Institute for Soldier Nanotechnologies under Contract ARO69680-18 with the U.S. Army Research Office.

-
- [1] K. Weinberg and M. Ortiz, Shock wave induced damage in kidney tissue, *Comput. Mater. Sci.* **32**, 588 (2005).
- [2] P. Movahed, W. Kreider, A. D. Maxwell, S. B. Hutchens, and J. B. Freund, Cavitation-induced damage of soft materials by focused ultrasound bursts: A fracture-based bubble dynamics model, *J. Acoust. Soc. Am.* **140**, 1374 (2016).
- [3] J. E. Lingeman, Extracorporeal shock wave lithotripsy: Development, instrumentation, and current status, *Urol. Clin. North Am.* **24**, 185 (1997).
- [4] M. Bailey, J. Mcateer, Y. Pishchalnikov, M. Hamilton, and T. Colonius, Progress in lithotripsy research, *Acoustics Today* **2**, 18 (2006).
- [5] T. J. Dubinsky, T. D. Khokhlova, V. Khokhlova, and G. R. Schade, Histotripsy: The next generation of high-intensity focused ultrasound for focal prostate cancer therapy, *J. Ultrasound Med.* **39**, 1057 (2020).
- [6] A. Hendricks-Wenger, L. Arnold, J. Gannon, A. Simon, N. Singh, H. Sheppard, M. A. Nagai-Singer, K. M. Imran, K. Lee, S. Clark-Deener, C. Byron, M. R. Edwards, M. M. Larson, J. H. Rossmeis, S. L. Coutermarsh-Ott, K. Eden, N. Dervis, S. Klahn, J. Tuohy, I. C. Allen *et al.*, Histotripsy ablation in preclinical animal models of cancer and spontaneous tumors in veterinary patients: A review, *IEEE Trans. Ultrason. Ferroelectr. Freq. Control* **69**, 5 (2022).
- [7] A. Hendricks-Wenger, R. Hutchison, E. Vlasisavljevich, and I. C. Allen, Immunological effects of histotripsy for cancer therapy, *Front. Oncol.* **11**, 681629 (2021).
- [8] A. Jean, M. Nyein, J. Zheng, D. Moore, J. Joannopoulos, and R. Radovitzky, An animal-to-human scaling law for blast-induced traumatic brain injury risk assessment, *Proc. Natl. Acad. Sci. USA* **111**, 15310 (2014).
- [9] J. Cummings, M. Aivazis, R. Samtaney, R. Radovitzky, S. Mauch, and D. Meiron, A virtual test facility for the simulation of dynamic response in materials, *J. Supercomput.* **23**, 39 (2002).
- [10] C. Franck, Microcavitation: The key to modeling blast traumatic brain injury? *Concussion* **2**, CNC47 (2017).
- [11] S. Mora, T. Phou, J. M. Fromental, and Y. Pomeau, Gravity Driven Instability in Elastic Solid Layers, *Phys. Rev. Lett.* **113**, 178301 (2014).
- [12] D. Riccobelli and P. Ciarletta, Rayleigh-Taylor instability in soft elastic layers, *Philos. Trans. R. Soc. A* **375** (2017).
- [13] A. Chakrabarti, S. Mora, F. Richard, T. Phou, F. Jean-Marc, Y. Pomeau, and B. Audoly, Selection of hexagonal buckling patterns by the elastic rayleigh-taylor instability, *J. Mech. Phys. Solids* **121**, 234 (2018).
- [14] G. Bevilacqua, X. Shao, J. R. Saylor, J. B. Bostwick, and P. Ciarletta, Faraday waves in soft elastic solids, *Proc. R. Soc. A* **476**, 20200129 (2020).
- [15] F. Hamaguchi and K. Ando, Linear oscillation of gas bubbles in a viscoelastic material under ultrasound irradiation, *Phys. Fluids* **27**, 113103 (2015).
- [16] K. Murakami, R. Gaudron, and E. Johnsen, Shape stability of a gas bubble in a soft solid, *Ultrason. Sonochemistry* **67**, 105170 (2020).
- [17] K. Murakami, Spherical and non-spherical bubble dynamics in soft matter, Ph.D. thesis, The University of Michigan, 2020.
- [18] A. López Ortega, M. Lombardini, P. T. Barton, D. I. Pullin, and D. I. Meiron, Richtmyer-Meshkov instability for elastic-plastic solids in converging geometries, *J. Mech. Phys. Solids* **76**, 291 (2015).
- [19] Y. B. Sun, J. J. Tao, R. H. Zeng, and X. T. He, Effects of viscosity and elasticity on the Richtmyer-Meshkov instability, *Phys. Rev. E* **98**, 033102 (2018).
- [20] Y. B. Sun, R. H. Zeng, and J. J. Tao, Elastic rayleigh-taylor and Richtmyer-Mmeshkov instabilities in spherical geometry, *Phys. Fluids* **32**, 124101 (2020).
- [21] J. Yang, A. Tzoumaka, K. Murakami, E. Johnsen, D. L. Henann, and C. Franck, Predicting complex nonspherical instability shapes of inertial cavitation bubbles in viscoelastic soft matter, *Phys. Rev. E* **104**, 045108 (2021).
- [22] L. Pociavsek, R. Dellsy, A. Kern, S. Johnson, B. Lin, K. Y. C. Lee, and E. Cerda, Stress and fold localization in thin elastic membranes, *Science* **320**, 912 (2008).

- [23] R. D. Richtmyer, Taylor instability in shock acceleration of compressible fluids, *Commun. Pure Appl. Math.* **13**, 297 (1960).
- [24] E. E. Meshkov, Instability of the interface of two gases accelerated by a shock wave, *Fluid Dyn.* **4**, 101 (1969).
- [25] T. Pezeril, G. Saini, D. Veysset, S. Kooi, P. Fidkowski, R. Radovitzky, and K. A. Nelson, Direct Visualization of Laser-Driven Focusing Shock Waves, *Phys. Rev. Lett.* **106**, 214503 (2011).
- [26] D. Martynowych, Materials in extreme conditions: Experimental developments and studies of systems far from equilibrium, Ph.D. thesis, Massachusetts Institute of Technology, 2021.
- [27] D. Veysset, U. Gutiérrez-Hernández, L. Dresselhaus-Cooper, F. De Colle, S. Kooi, K. A. Nelson, P. A. Quinto-Su, and T. Pezeril, Single-bubble and multibubble cavitation in water triggered by laser-driven focusing shock waves, *Phys. Rev. E* **97**, 053112 (2018).
- [28] B. Saintyves, O. Dauchot, and E. Bouchaud, Bulk Elastic Fingering Instability in Hele-Shaw Cells, *Phys. Rev. Lett.* **111**, 047801 (2013).
- [29] The **ΣMIT** Development Group, **ΣMIT**, a scalable computational framework for large-scale simulation of complex mechanical response of materials (2021).
- [30] Y.-H. Li, Equation of state of water and sea water, *J. Geophys. Res.* **72**, 2665 (1967).
- [31] S. Mora, M. Abkarian, H. Tabuteau, and Y. Pomeau, Surface instability of soft solids under strain, *Soft Matter* **7**, 10612 (2011).
- [32] P. Ciarletta, Wrinkle-to-fold transition in soft layers under equibiaxial strain: A weakly nonlinear analysis, *J. Mech. Phys. Solids* **73**, 118 (2014).
- [33] S. Lin, Y. Mao, H. Yuk, and X. Zhao, Material-stiffening suppresses elastic fingering and fringe instabilities, *Int. J. Solids Struct.* **139-140**, 96 (2018).
- [34] J. S. Biggins and L. Mahadevan, Meniscus instabilities in thin elastic layers, *Soft Matter* **14**, 7680 (2018).
- [35] B. Giovanardi, A. A. Sliwiak, A. Koshakji, S. Lin, X. Zhao, and R. Radovitzky, A path-following simulation-based study of elastic instabilities in nearly-incompressible confined cylinders under tension, *J. Mech. Phys. Solids* **131**, 252 (2019).
- [36] J. B. Keller and M. Miksis, Bubble oscillations of large amplitude, *J. Acoust. Soc. Am.* **68**, 628 (1980).
- [37] J. B. Estrada, C. Barajas, D. L. Henann, E. Johnsen, and C. Franck, High strain-rate soft material characterization via inertial cavitation, *J. Mech. Phys. Solids* **112**, 291 (2018).
- [38] M. Versluis, B. Schmitz, A. von der Heydt, and D. Lohse, How snapping shrimp snap: Through cavitating bubbles, *Science* **289**, 2114 (2000).
- [39] A. Lew, R. Radovitzky, and M. Ortiz, An artificial-viscosity method for the Lagrangian analysis of shocks in solids with strength on unstructured, arbitrary-order tetrahedral meshes, *J. Comput.-Aided Mater. Des.* **8**, 213 (2001).
- [40] K.-J. Bathe, *Finite Element Procedures* (Prentice Hall, Hoboken, NJ, 1996).
- [41] C. Kane, J. E. Marsden, M. Ortiz, and M. West, Variational integrators and the Newmark algorithm for conservative and dissipative mechanical systems, *Int. J. Numer. Methods Eng.* **49**, 1295 (2000).
- [42] See Supplemental Material at <http://link.aps.org/supplemental/10.1103/PhysRevE.107.L022601> for animated videos of the simulation results as well as an instability order parameter study.
- [43] J. P. Sauppe, S. Palaniyappan, B. J. Tobias, J. L. Kline, K. A. Flippo, O. L. Landen, D. Shvarts, S. H. Batha, P. A. Bradley, E. N. Loomis, N. N. Vazirani, C. F. Kawaguchi, L. Kot, D. W. Schmidt, T. H. Day, A. B. Zylstra, and E. Malka, Demonstration of Scale-Invariant Rayleigh-Taylor Instability Growth in Laser-Driven Cylindrical Implosion Experiments, *Phys. Rev. Lett.* **124**, 185003 (2020).
- [44] V. A. Smalyuk, J. A. Delettrez, V. N. Goncharov, F. J. Marshall, D. D. Meyerhofer, S. P. Regan, T. C. Sangster, R. P. J. Town, and B. Yaakobi, Rayleigh-Taylor instability in the deceleration phase of spherical implosion experiments, *Phys. Plasmas* **9**, 2738 (2002).
- [45] D. L. Tubbs, C. W. Barnes, J. B. Beck, N. M. Hoffman, J. A. Oertel, R. G. Watt, T. Boehly, D. Bradley, P. Jaanimagi, and J. Knauer, Cylindrical implosion experiments using laser direct drive, *Phys. Plasmas* **6**, 2095 (1999).
- [46] R. Betti, K. Anderson, V. N. Goncharov, R. L. McCrory, D. D. Meyerhofer, S. Skupsky, and R. P. J. Town, Deceleration phase of inertial confinement fusion implosions, *Phys. Plasmas* **9**, 2277 (2002).
- [47] J. P. Sauppe, S. Palaniyappan, E. N. Loomis, J. L. Kline, K. A. Flippo, and B. Srinivasan, Using cylindrical implosions to investigate hydrodynamic instabilities in convergent geometry, *Matter and Radiation at Extremes* **4**, 065403 (2019).
- [48] M. A. Biot, Surface instability of rubber in compression, *Appl. Sci. Res., Sect. A* **12**, 168 (1963).
- [49] G. I. Taylor, The instability of liquid surfaces when accelerated in a direction perpendicular to their planes. I, *Proc. R. Soc. London A* **201**, 192 (1950).
- [50] G. I. Bell, Taylor instability on cylinders and spheres in the small amplitude approximation, Tech. Rep. No. LA-1321 (Los Alamos Scientific Laboratory of the University of California, 1951).
- [51] Y. Zhang, X. Du, H. Xian, and Y. Wu, Instability of interfaces of gas bubbles in liquids under acoustic excitation with dual frequency, *Ultrason. Sonochemistry* **23**, 16 (2015).
- [52] K. Klapcsik and F. Hegedus, Study of non-spherical bubble oscillations under acoustic irradiation in viscous liquid, *Ultrason. Sonochemistry* **54**, 256 (2019).
- [53] A. Prosperetti, Viscous effects on perturbed spherical flows, *Q. Appl. Math.* **34**, 339 (1977).
- [54] A. Francescutto and R. Nabergoj, Pulsation amplitude threshold for surface waves on oscillating bubbles, *Acustica* **41**, 215 (1978).
- [55] G. I. Barenblatt, *Scaling*, Cambridge Texts in Applied Mathematics (Cambridge University Press, Cambridge, 2003).
- [56] A. R. Piriz, J. J. López Cela, N. A. Tahir, and D. H. H. Hoffmann, Richtmyer-Meshkov instability in elastic-plastic media, *Phys. Rev. E* **78**, 056401 (2008).
- [57] Y. B. Sun, R. H. Zeng, and J. J. Tao, Effects of viscosity and elasticity on Rayleigh-Taylor instability in a cylindrical geometry, *Phys. Plasmas* **28**, 062701 (2021).
- [58] H. Yu and D. Livescu, Rayleigh-Taylor instability in cylindrical geometry with compressible fluids, *Phys. Fluids* **20**, 104103 (2008).

- [59] M. Versluis, D. E. Goertz, P. Palanchon, I. L. Heitman, S. M. van der Meer, B. Dollet, N. de Jong, and D. Lohse, Microbubble shape oscillations excited through ultrasonic parametric driving, *Phys. Rev. E* **82**, 026321 (2010).
- [60] Q. Zhang and M. J. Graham, A numerical study of Richtmyer-Meshkov instability driven by cylindrical shocks, *Phys. Fluids* **10**, 974 (1998).
- [61] J. Ball, Discontinuous equilibrium solutions and cavitation in nonlinear elasticity, *Philos. Trans. R. Soc. A* **306**, 557 (1982).
- [62] C. W. Barney, C. E. Dougan, K. R. McLeod, A. Kazemi-Moridani, Y. Zheng, Z. Ye, S. Tiwari, I. Sacligil, R. A. Riggelman, S. Cai, J.-H. Lee, S. R. Peyton, G. N. Tew, and A. J. Crosby, Cavitation in soft matter, *Proc. Natl. Acad. Sci.* **117**, 9157 (2020).